NANO · MICRO small
www.small-journal.com

Construction of Hierarchical Films via Layer-by-Layer Assembly of Exfoliated Unilamellar Zeolite Nanosheets

*Chenhui Wang, Nobuyuki Sakai, Yasuo Ebina, Takayuki Kikuchi, Justyna Grzybek, Wieslaw J. Roth, Barbara Gil, Renzhi Ma, and Takayoshi Sasaki**

Zeolites have been widely applied as versatile catalysts, sorbents, and ion exchangers with unique porous structures showing molecular sieving capability. In these years, it is reported that some layered zeolites can be delaminated into molecularly thin 2-dimensional (2D) nanosheets characterized by inherent porous structures and highly exposed active sites. In the present study, two types of zeolite nanosheets with distinct porous structures with MWW topology (denoted mww) and ferrierite-related structure (denoted bifer) are deposited on a substrate through the solution process via electrostatic self-assembly. Alternate deposition of zeolite nanosheets with polycation under optimized conditions allows the layer-by-layer growth of their multilayer films with a stacking distance of 2–3 nm. Furthermore, various hierarchical structures defined at the unit-cell dimensions can be constructed simply by conducting the deposition of mww and bifer nanosheets in a designed sequence. Adsorption of a dye, Rhodamine B, in these films, is examined to show that adsorption is dependent on constituent zeolite nanosheets and their assembled nanostructures. This work has provided fundamental advancements in the fabrication of artificial zeolite-related hierarchical structures, which may be extended to other zeolite nanosheets, broadening their functionalities, applications, and benefits.

1. Introduction

Soft-chemical process of delaminating/exfoliating layered materials into unilamellar nanosheets dispersed in solution and reassembling them as building blocks is one of the most effective approaches for designing and fabricating advanced nanostructured materials with desired functionality.[1–6] The tailored structures and specific properties associated with them can be constructed by precisely controlling the arrangements of selected nanosheets or other components at a molecular scale. It has been reported that a range of homo- or hetero-multilayer films consisting of various 2D nanosheets can be constructed layer-by-layer on a support through mechanical transfer,[7] sequential adsorption,[8–10] spin-coating,[11–13] one drop assembly,[14] and Langmuir–Blodgett deposition.[15–17] The latter four are based on the solution processes, which are suitable for facile fabrication of centimeter-wide films. The supports for layer-by-layer assembly can be flat substrates with smooth or rough surfaces or even polymer beads in various sizes,[17–19] and the film thickness can be controlled stepwise at the nanoscale range by the number of deposition cycles. The superlattice-like structures of alternately restacked different nanosheets can be successfully constructed by this simple procedure, providing new and enhanced functionalities, useful for ferroelectric/dielectrics,[20,21] photocatalysis,[22–25] electrocatalysis,[26–28] photo- and electrochemical energy storage,[29–33] and photoluminescence.[34,35] Thus, layer-by-layer assembly has been proven to be a versatile and powerful method to develop functional materials with precisely controllable designed structures. A wide range of colloidal 2D nanosheets such as graphene, chalcogenides, oxides, and hydroxides are available as building blocks for these processes,[3,4,36,37] demonstrating high potential for achieving advanced functionalities and applications. Thus, it is of significant importance to extend the application of the layer-by-layer assembly technique to novel nanosheets as building blocks, which may create unique materials and achieve sophisticated applications.

Zeolites possess diverse structures with well-defined porous frameworks, which have been widely used as industrial catalysts and adsorbents.[38–42] Intensive efforts have been devoted to the synthesis of new zeolite frameworks with improved performance.[43,44] However, there are still limitations in achieving tailored pore size, accessibility of active sites, and structure diversity.[45,46] The traditional zeolites have extended 3D structures, but ≈10% of them have been shown to have a second

C. Wang, N. Sakai, Y. Ebina, T. Kikuchi, R. Ma, T. Sasaki
Research Center for Materials Nanoarchitectonics (MANA)
National Institute for Materials Science (NIMS)
1-1 Namiki, Tsukuba, Ibaraki 305-0044, Japan
E-mail: sasaki.takayoshi@nims.go.jp
J. Grzybek, W. J. Roth, B. Gil
Faculty of Chemistry
Jagiellonian University
Gronostajowa 2, Kraków 30–387, Poland

The ORCID identification number(s) for the author(s) of this article can be found under https://doi.org/10.1002/smll.202308293

DOI: 10.1002/smll.202308293

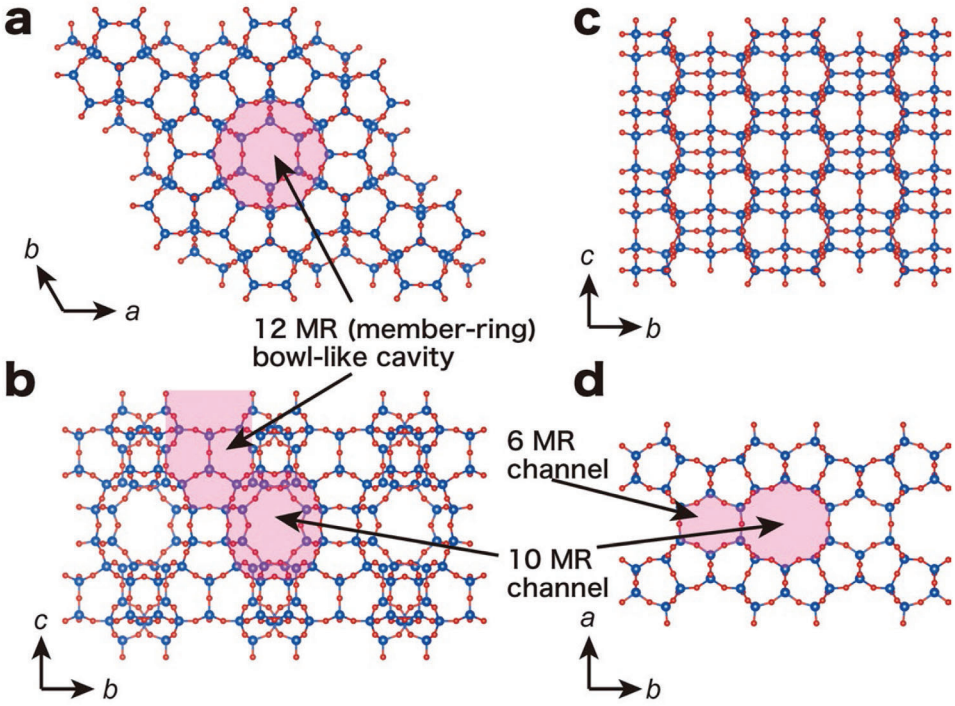

Figure 1. Top and side views of the structures for a,b) mww nanosheets and c,d) bifer nanosheets represented by the FER structure.

form, consisting of layers that can condense into the extended 3D framework.[47] These unique classes of layered zeolites are expected to break through the limitations of the traditional 3D forms.[47–50] In particular, if they are exfoliated into single layers, the resulting products, or unilamellar zeolite nanosheets, are molecularly thin with a very high aspect ratio and ultimate exposure of active sites.[51,52] In contrast to the other known 2D nanosheets, the zeolite ones can have internal open channels, which provide unique properties and opportunities. For example, such open channels facilitate the transport of ions and molecules especially across the nanosheets, which has been a big obstacle for other 2D materials due to absence of channels/pores. On the basis of these advantages, 2D zeolite nanosheets can be envisioned for promising applications, such as sensing, adsorption, storage, catalysis, separation, and others, wherein abundant active sites and fast diffusion of ions/molecules can play important roles in enhancing their performance.

Recently, we have reported the preparation of two kinds of high-quality zeolite nanosheets with MWW topology (denoted mww)[53] and a ferrierite-related structure (denoted bifer)[54] by exfoliating the corresponding layered zeolites into colloidal solutions of single layers. Zeolite MWW is commercially used for catalytic alkylation of aromatics and its framework structure is well-known.[47,55,56] The structure of bifer is unknown but its unit cell is similar to the zeolite ferrierite and it is prepared with the template, choline, that is also known to produce ferrierite layers.[54,57] Recently reported zeolite ECNU-28 shows X-ray diffraction (XRD) data and other features similar to bifer but has been assigned the framework topology SZR with a cross-section similar to ferrierite.[58] The relationship between bifer and ECNU-28 and their exact structure remain to be elucidated.

Figure 1 depicts the 2D porous structures of MWW and FER as a possible model for bifer. It is possible to tailor various hierarchical zeolite-based materials using zeolite nanosheets as building blocks, which is exemplified by ≈15 different architectures obtained with zeolite MWW layers.[50,52] Exfoliated nanosheets allow combining different frameworks together at the unit cell level and further expand the zeolite library and its applications. Its concrete benefits are demonstrated by the reported mixture of bifer and mww layers[54] and mixed zeolite hybrids of mww layers and zeolite MFI.[59] The hybrid zeolites exhibit an enhanced catalytic activity in a model reaction by showing conversions greater than the sum of each component alone. A particularly notable capability enabled by exfoliated zeolite nanosheets in comparison to the standard crystals is a top-down assembly into films and self-standing discs.[53,60] This has a wide range of possibilities but has been rarely reported so far, mainly due to the relative novelty of such liquid zeolite systems.

In this work, multilayer films of zeolite nanosheets of mww, bifer, and their composites of different stacking order are fabricated by the layer-by-layer assembly process, which involves alternate adsorption/deposition of cationic polymers and zeolite nanosheets. The optimized parameters for the assembly can achieve regular deposition of zeolite nanosheets. The layer-by-layer film growth is demonstrated by monitoring FT-IR spectroscopy and X-ray diffraction (XRD) measurement/simulation. Various hierarchical nanostructures can be designed by this solution process. The adsorption behavior of the fabricated films to dye molecules of Rhodamine B is examined, as an example for their applications. This work has provided a solid foundation for the design of new zeolites based onmolecularly thin zeolite nanosheets as 2D building blocks, which will greatly enrich the

material library and exhibit huge potential for promising applications.

2. Results and Discussion

2.1. Preparation of mww and bifer Nanosheets

Layered zeolites designated as MCM-56 and Al-ZSM-55, which contain the mww and bifer layers, respectively, are prepared according to the previous reports.[53,54] The obtained MCM-56 is composed of grains of several micrometers in size (Figure S1a, Supporting Information). Al-ZSM-55 is a mixture of 2 phases, unexfoliable zeolite precursor (formally ZSM-55 producing zeolite CDO upon calcination) composed of fer layers, 0.9 nm thick, and exfoliating bifer layers which are 1.8 nm thick.[57] The Al-ZSM-55 sample is obtained as platy microcrystals (Figure S1b, Supporting Information). The XRD pattern of MCM-56 can be indexed to the hexagonal structure of the mww topological framework (Figure S2a, Supporting Information).[61] The orthorhombic unit cell of bifer is similar to that of ferrierite, FER, as well as CDO and SZR zeolite frameworks (XRD shown in Figure S2b, Supporting Information),[57] but its exact structure is unknown.

The zeolite nanosheets of mww and bifer are prepared via delamination of the layered zeolites MCM-56 and Al-ZSM-55, respectively, through a soft-chemical route via osmotic swelling with tetrabutylammonium hydroxide solution (see Experimental Section for details). Unilamellar nanosheets are separated from the unexfoliated material via centrifugation of crude suspensions at an appropriate rotation speed. To optimize conditions for collecting unilamellar nanosheets, the samples recovered at different rotation speeds are characterized by atomic force microscopy (AFM) observation (Figure S3, Supporting Information). The solutions obtained from layered zeolites of MCM-56 and Al-ZSM-55 are centrifuged at 20 and 10 krpm, respectively, producing turbid suspensions at the top and sediments at the bottom. The top suspensions are separated and centrifuged at higher rotation speeds of 30 and 20 k rpm, bringing about total sedimentation of the dispersed nanosheets. The recovered glue-like sediments are redispersed in water to produce the suspensions of mww and bifer nanosheets (**Figure 2**). These suspensions are appropriately diluted and deposited on a Si wafer chip. As observed by AFM in Figure 2, many sheet-like objects with a lateral size of ≈0.2 and 0.4 μm are observed, respectively. Their thickness is ≈2.5 and 2.1 nm, being consistent with that for unilamellar mww and bifer nanosheets reported.[53,54]

In-plane XRD data are collected for monolayer films for each sample on Si supports. Sharp diffraction peaks indicate the highly crystalline nature of the nanosheets (Figure S4, Supporting Information). The peaks can be indexed in terms of 2D hexagonal and rectangular lattices for mww and bifer, respectively. The unit cell dimensions are refined as a = 1.4284(8) nm for the former and b = 1.4642(6) nm × c = 0.7450(1) nm for the latter. The a parameter for mww is very close to the in-plane lattice parameters of the precursory MCM-56,[47] indicating that the host layer architecture is preserved after exfoliation into the unilamellar nanosheets. The 3D structure, i.e., framework topology, of bifer is not known, but presumably, its internal layer

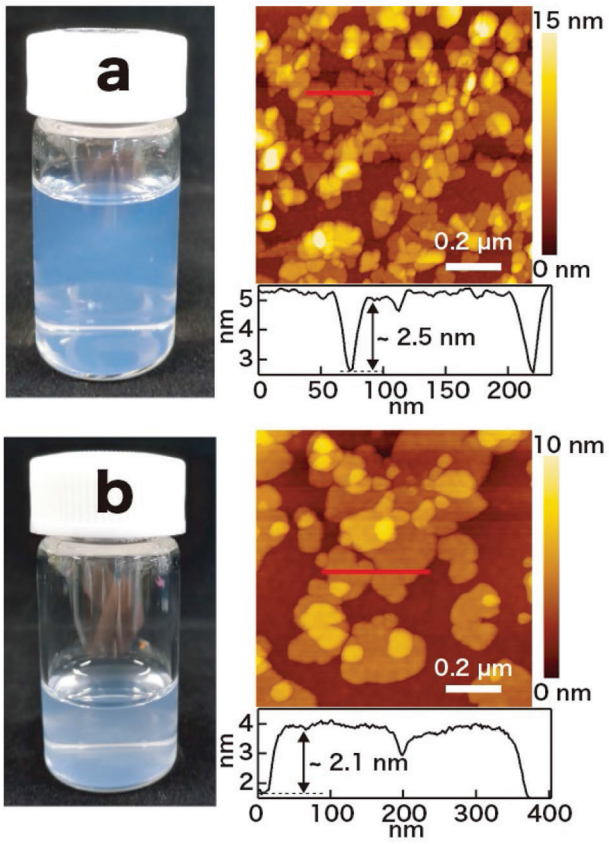

Figure 2. Photographs of colloidal suspensions of a) mww and b) bifer nanosheets and corresponding AFM images. The height profiles are obtained along the red lines indicated in the AFM images.

architecture is preserved upon exfoliation. The obtained mww nanosheets with the unilamellar thickness possess horizontal intralayer 10-member-ring (MR) channels and vertical open bowl-like cavities, with a diameter of 12-MR aperture and a depth of 0.7 nm, on the surface (Figure 1a,b).[55] On the other hand, the bifer unilamellar sheets are initially analyzed based on the FER or CDO structure. Our previous study suggests the FER structure as more likely, i.e., containing alternating 10- and 6-MR channels parallel to the lateral direction and 8-MR channels perpendicular to these two channels (Figure 1c,d).[54] As shown in Figure 2, the mww and bifer nanosheets are well dispersed as colloidal suspensions with an opalescent appearance. Their zeta potentials are measured to be −30 and −32 mV (Figure S5, Supporting Information), indicating their negatively charged nature.

2.2. Deposition of Zeolite Nanosheets on a Substrate

Deposition of these zeolite nanosheets on a substrate is examined. Since the nanosheets are negatively charged, polycations such as poly(diallyldimethylammonium) chloride (PDDA) are employed to facilitate adsorption by electrostatic attraction. In the first step, a cleaned Si wafer substrate is primed with PDDA to turn the surface positively charged and, in the subsequent process, it is immersed in a colloidal suspension of the zeolite

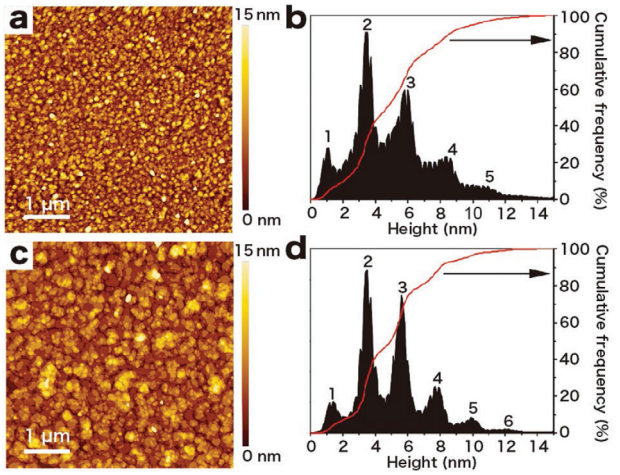

Figure 3. AFM images a,c) and corresponding height histograms b,d) of the Si substrate surface after deposition of mww and bifer nanosheets, respectively. The deposition time is 15 min and the nanosheet concentration is 0.08 and 0.12 g dm^{-3}, respectively.

nanosheets. The nanosheet concentration and deposition time are studied as key deposition parameters. The resulting film samples are observed by AFM, to gain information on how the zeolite nanosheets are deposited. **Figure 3**a,c depicts AFM images of the samples after adsorbing the nanosheets under typical conditions. It is obvious that the substrate surface is densely covered with nanosheets. As shown in Figure 3b,d, the histogram is composed of multiple peaks at 1.1, 3.4, 5.7, 8.1, 10.5 nm for mww and 1.3, 3.5, 5.6, 7.7, 9.8, and 12.0 nm for bifer. Note that the peak intervals roughly correspond to each nanosheet thickness. This indicates that the first peak with the smallest height, the second peak, and the following peaks should represent the regions uncovered by the zeolite, i.e., bare Si surface, covered by monolayer nanosheets, and by multiple overlapped nanosheets, respectively. The relative abundance of each area is estimated to assess how the nanosheets are adsorbed on the substrate. Through such analysis of films fabricated with various deposition parameters (Figures S6–S9, Supporting Information), the optimum deposition time and concentration are determined under the criteria to achieve a larger monolayer area as well as a smaller uncovered region (Figure S10, Supporting Information). The optimum deposition parameters chosen are 15 min and 0.08 g cm^{-3} for the mww film fabrication, and 15 min and 0.12 g cm^{-3} for the bifer film (Figure 3). The difference between these optimum conditions may reflect the different lateral sizes, thicknesses, and charge densities of the mww and bifer nanosheets. Under these optimum parameters, the ratio of the uncovered gap and the covered region in a monolayer, bilayer, and tri-layer are ≈12%, ≈38%, ≈34%, and ≈15% with mww nanosheets, respectively, while ≈8%, ≈36%, ≈33%, and ≈14% with bifer nanosheets. This film architecture may look rather disorganized, but actually, similar film quality has been reported for films of other 2D materials such as metal oxide nanosheets.[9,10] The formation of uncovered regions and overlapped areas is inevitable for such self-assembly processes with 2D materials possessing submicrometer-scale lateral dimensions.

2.3. Multilayer Build-Up of Zeolite Nanosheets

Having the optimized parameters, multilayer films of zeolite nanosheets are constructed by alternately depositing zeolite nanosheets and PDDA layers, which is similar to the multilayer build-up of metal oxide nanosheets.[8–10] The layer-by-layer deposition is monitored by Fourier transform infrared (FT-IR) spectroscopy. The mww and bifer nanosheets exhibit absorption bands in the wavenumber range of 1000–1100 cm^{-1} (**Figure 4**a,b), which are ascribed to the antisymmetric stretching vibration Si-O—Si between tetrahedra.[62,63] This band is triple degenerated, due to the presence of three oscillators (3N-6). All three vibrations are active in IR. The maximum at 1058 cm^{-1} is very symmetric, suggesting the absence of the maxima derived from Si—O—Al bridges, due to low Al content for bifer.[64] The absorbance increases linearly with the number of deposition cycles for both cases (Figure 4c). This indicates that a nearly equal amount of nanosheets was deposited in each cycle, demonstrating the successful growth of multilayer films of zeolite nanosheets. The absorbance increment per layer is 0.0060 at 1072 cm^{-1} and 0.0114 at 1058 cm^{-1} for mww and bifer films, respectively.

The fabricated multilayer films are further characterized by XRD analysis (**Figure 5**). The ten-layer mww film exhibits two peaks at 2.6° and 5.7°, which are indexed to the 001 and 002 reflections from the restacked structure with the intersheet spacing of 3.4 nm (Figure 5a). This value can be reasonably explained in terms of the stacked mww nanosheets (2.5 nm in thickness) accommodating PDDA between them. On the other hand, the ten-layer bifer film shows two basal peaks at 3.5° and 7.3°, indicating the intersheet spacing of 2.5 nm (Figure 5b), which is again consistent with the multilayer structure of bifer nanosheets (2.1 nm in thickness) with intercalated PDDA.

Furthermore, a simulation of basal diffraction series has been conducted based on the ten-layer multilayer structures. The simulated profiles (red line) are generally in accord with the experimental XRD pattern (blue) in terms of the peak position (Figure 5; Figure S11, Supporting Information), confirming the ordered layered structures based on the building blocks of monolayer mww and bifer nanosheets. The sharp basal peaks from the ideal structures appear together with the Laue ripple peaks (Figure S11a,e, Supporting Information). The broad nature of the observed patterns should be ascribed to some structural disorder as can be deduced from the deposition behavior of the nanosheets giving uncovered gaps and overlapped patches besides the ideal monolayer region. Such a broadening effect is taken into account by applying the lattice distortion parameter, α, in Equation (1) (see Experimental section). Then a better fit is obtained with $\alpha = 0.39$ nm and 0.24 nm, for the films of mww and bifer nanosheet, respectively (Figure 5 and Figure S11c,g, Supporting Information).

2.4. Heating of Multilayer Films of Zeolite Nanosheets

Figure 6 depicts XRD data of the multilayer films of mww and bifer nanosheets before and after the heat treatment at 400 °C. Simulations confirm (Figures S12 and S13, Supporting Information) that the stacked multilayer structures remain substan-

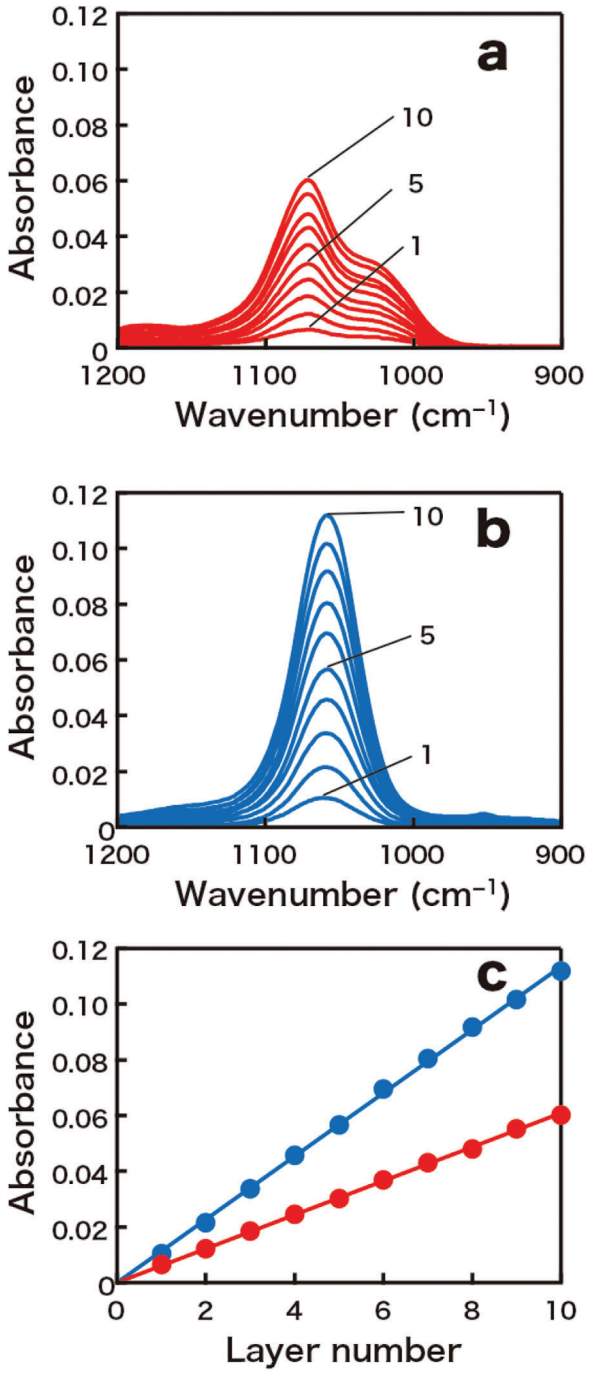

Figure 4. FT-IR spectra showing the build-up process of multilayer films of a) mww and b) bifer nanosheets on a Si wafer. c) Absorbance at 1072 cm^{-1} (mww, red) and 1058 cm^{-1} (bifer, blue) plotted against the number of repeating cycles.

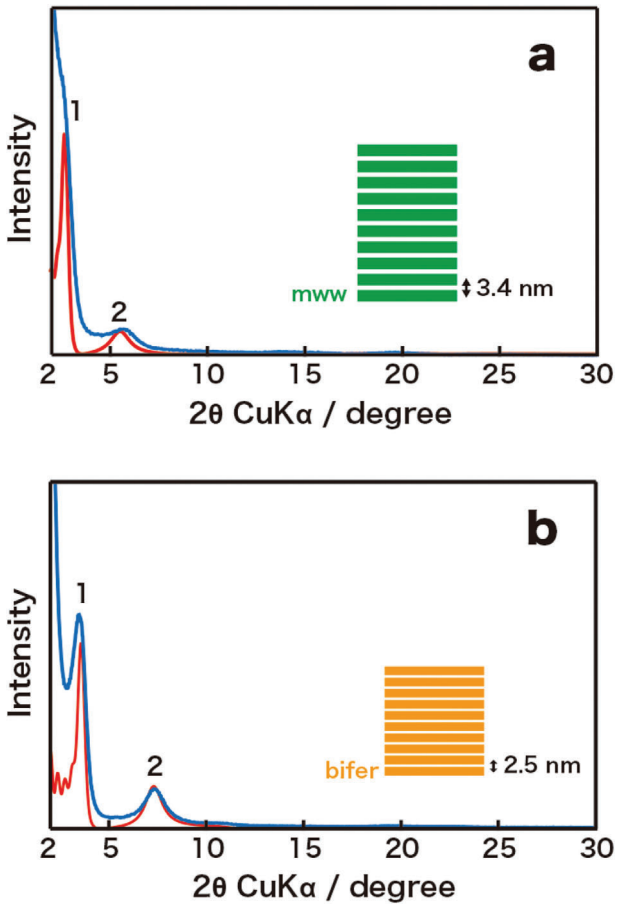

Figure 5. The measured (blue line) and simulated (red line) XRD patterns of a) mww and b) bifer nanosheets. The numbers indicate the reflection orders. Simulation parameters are $N = 10$, $\alpha = 0.39$ nm, and $N = 10$, $\alpha = 0.24$ nm, respectively.

tially unchanged except for the intersheet shrinkage; from 3.4 to 2.3 nm for the mww film and from 2.5 to 1.8 nm for the bifer. The removal of interlayer inclusions through the combustion of PDDA should be responsible for this contraction. Similar magnitudes of shrinkage are observed for multilayer films composed of oxide nanosheets and polycations.[65]

It is important to point out that the resulting repeating distances, 2.3 nm for mww and 1.8 nm for bifer, are somewhat shorter than the apparent layer thickness values based on 3D zeolite structures, MWW and FER zeolites, with *c*-axis lengths equal to 2.520 and 1.8708 nm, respectively.[47,66] This shorter repeating distance can be explained by failure in perfect topotactic condensation of neighboring nanosheets. The surface silanols and oxygen atoms of the neighboring nanosheets can be interdigitated. Layered zeolite materials with an interlayer distance shorter than the theoretical layer thickness have been reported earlier and denoted "sub-zeolites".[57] Considering the layer-by-layer assembly process from colloidal suspension, it is reasonable to expect that the nanosheets will be preferentially restacked without making a regular sheet-to-sheet registry, making the perfect 3D condensation difficult.

2.5. Heteroassembled Films

Layer-by-layer deposition of multiple zeolite nanosheets in various sequences may produce artificial or superlattice zeolites, bringing about a new diversity of structures, properties, and functions of zeolites with emergent applications and performance. As

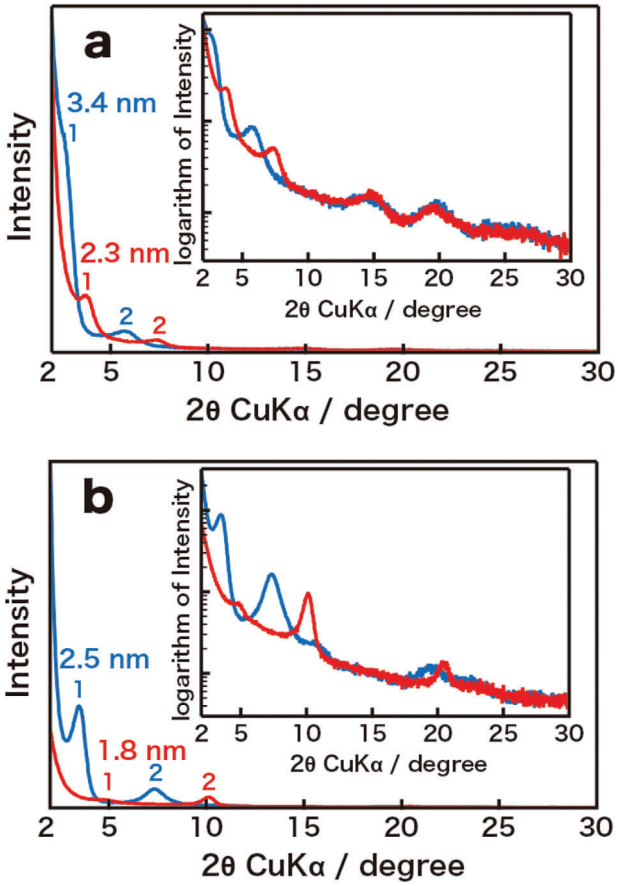

Figure 6. XRD patterns of as-fabricated (blue line) and heated to 400 °C (red line) multilayer films of a) mww and b) bifer nanosheets.

a demonstration, three kinds of heteroassembled films with the unit of $(mww/bifer)_6$, $(mww_2/bifer_2)_3$, and $(mww_3/bifer_3)_2$ are fabricated by repeating the immersion processes in the designed sequences. The growth of these films was monitored by FT-IR spectra (**Figure 7**). The absorbance increases with the number of layers for all samples. Importantly, the absorbance gain is dependent on which nanosheet is deposited in the cycle. Its magnitude is equal to the values observed in multilayer film growth for mww and bifer nanosheets; 0.0060 at 1072 cm^{-1} and 0.0114 at 1058 cm^{-1}, respectively. The deposition sequences of mww/bifer, $mww_2/bifer_2$, and $mww_3/bifer_3$ result in distinct modes of absorbance change, clearly confirming the successful formation of the heteroassembled films in the designed structures.

These are taken as new zeolites or mixed-layer zeolites, which cannot be obtained by conventional synthetic methods. The "hierarchical zeolites" have been reported recently.[67–69] These hierarchical zeolites/MOFs are directly synthesized in different morphological forms for different purposes, for example, nanoparticles, sheets/plates, and membranes for applications in catalysis, sensing, and gas separation, respectively. In contrast, the hierarchical structures reported in this study are defined at the unit-cell level, typically superlattice assemblies of mww and bifer nanosheets alternately stacked, which cannot be realized through any direct synthetic approach. The obtained ultrathin films/coatings are regarded as more favorable for ultrathin catalyst layers, high-precision and high-sensitivity sensors, etc.

Figure 8 depicts the XRD data for the superlattice films of $(mww/bifer)_6$ nanosheets. The experimental profile is extracted by subtracting a baseline based on the Sonneveld–Visser method[70] (Figure 8a). XRD simulation is then carried out based on the superlattice structure of alternate mww/bifer sequence in comparison with the random stacking model (Figures S12 and S13, Supporting Information). The experimental profile looks like an intermediate pattern between these two models, which may be reasonable considering the rather disordered adsorption of the nanosheets at each deposition step (Figure 8b). Figure S14 shows the cross-sectional TEM image of the alternately deposited film of $(mww/bifer)_5$. The lamellar fringes are observed and the total thickness of 28.9 nm is roughly consistent with an estimated value based on the thickness of the nanosheets and the film architecture. On the other hand, a regular alternate structure of mww and bifer nanosheets was not clearly resolved, which may be consistent with the XRD analysis above.

2.6. Dye Adsorption

Dye-adsorption capacities of multilayer films of mww and bifer nanosheets and their superlattice film of mww/bifer are examined. The films, heated at 400 °C, are immersed in an aqueous solution of a typical dye, Rhodamine B. After 1 day, the films are taken out, rinsed with copious amounts of water, and subject to measurements of UV–visible (UV–vis) absorption spectra. A clear absorption band at 567 nm, which is attributable to Rhodamine B, is detected in multilayer films of mww nanosheets and superlattice films of mww/bifer, while it is negligible for the films of bifer nanosheets (Figure S15, Supporting Information). **Figure 9** shows that the absorbance at 567 nm is almost linearly enhanced as a function of the mww layer number. The adsorption capacity is clearly dependent on the zeolite nanosheets and the film architecture.

The adsorption capacity of the multilayer films of mww nanosheets is estimated. Absorbance gain at the peak top (567 nm) is 0.006 per layer of mww nanosheets (Figure 9), considering two films on both sides of the glass substrate. Because the molar extinction coefficient of Rhodamine B at 553.5 nm is 1.05×10^5 mol^{-1} dm^3 cm^{-1} (Figure S16, Supporting Information), the amount of Rhodamine B adsorbed is calculated to be 5.83×10^{-11} mol cm^{-2}, which corresponds to 0.46 molecule per 2D unit cell area of the mww nanosheet. The mww nanosheet is featured with a vertical open bowl-like cavity of 0.7 nm in diameter and 0.7 nm in depth on its surface. This cavity space may accommodate one dye molecule per unit cell (Figure S17, Supporting Information). Note that the mww nanosheet does not have open channels across it, which means that vertical penetration of the Rhodamine B molecules in the restacked multilayer film is not allowed. Furthermore, horizontal 10 MR intrasheet channels are too small to take up the dye molecules. Thus, the dye molecules may migrate in the intersheet gallery to the cavity, where they are trapped mainly via electrostatic interaction.

The XRD data after the dye adsorption (Figure S18, Supporting Information) shows basal diffraction peaks with a stacking distance of 2.3 nm, which is the same as that before the treatment.

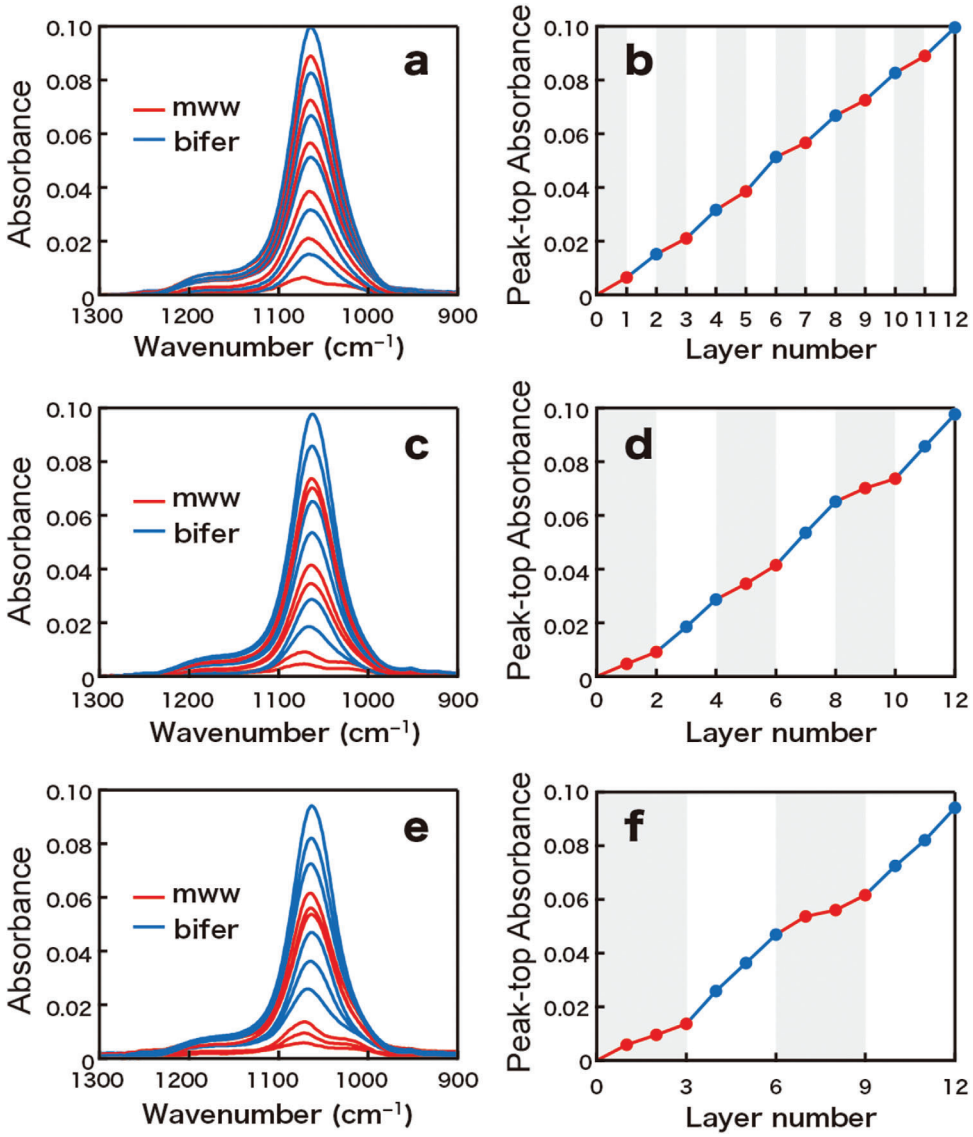

Figure 7. FT-IR absorption spectra in the construction process of heteroassembled multilayer films with a different repeating unit of a,b) mww/bifer, c,d) $mww_2/bifer_2$, and e,f) $mww_3/bifer_3$; the absorbance at ≈1072 cm^{-1} of the films. The red and blue traces and circles represent the deposition of mww and bifer nanosheets, respectively.

This suggests that the dye molecule is taken up into the cavity without altering the restacked structure. The uptake of Rhodamine B into the bulk 3D zeolite composed of ordered stacking of fused mww layers, MWW-22, has been reported,[71,72] and the adsorbed amount is estimated as 1.1×10^{-4} mol g^{-1}. The above value of 5.83×10^{-11} mol cm^{-2} calculated for the multilayer film produces 1.44×10^{-4} mol g^{-1}, upon conversion to unit mass, showing remarkable similarity between the bulk zeolite and film. This result clearly indicates that the dye adsorption takes place even in ultrathin films in a similar way to that in the bulk zeolite. This feature is important, expecting some advantageous applications of zeolite nanofilms.

The bifer multilayer film, on the other hand, does not adsorb Rhodamine B, apparently because of the absence of such void spaces on the nanosheet. The 6 and 10 MR channels are too small for the dye molecules. The heteroassembled superlattice film of mww/bifer, can provide the open cavities from mww nanosheets, although their population is half of that in the multilayer film. This may be responsible for the somewhat smaller adsorption capacity of Rhodamine B. These results are encouraging, suggesting that specific structural materials can be controllably fabricated to achieve specific functions through the layer-by-layer assembly, which greatly expands the scope beyond the capabilities of the conventional direct synthesis process.

3. Conclusion

We have successfully demonstrated the construction of artificial zeolite films with unique structures by employing molecularly thin zeolite nanosheets as building blocks. A substrate

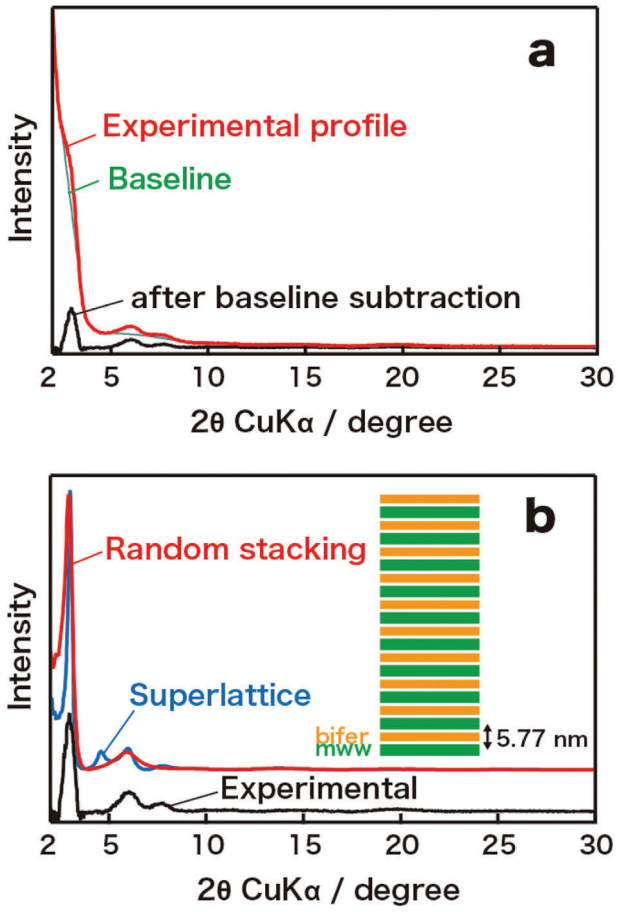

Figure 8. XRD patterns of a) experimental profile and b) simulated profile of superlattice films of mww/bifer nanosheets.

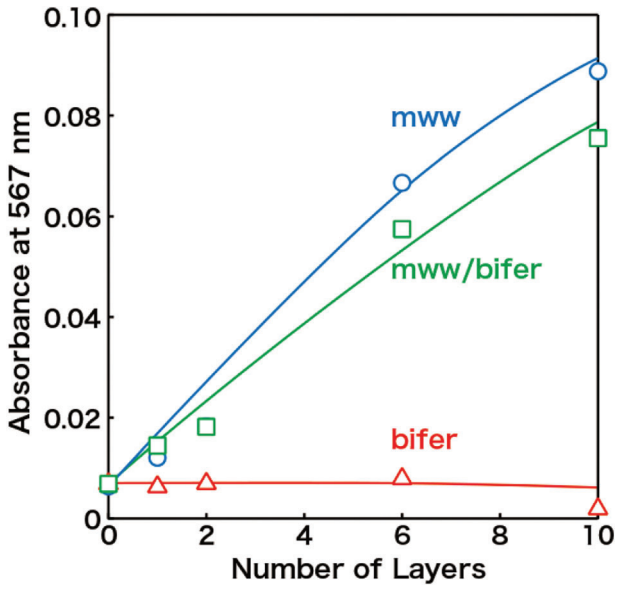

Figure 9. Absorbance at 567 nm for films of $(mww)_n$, $(bifer)_n$, and $(mww/bifer)_{n/2}$.

primed with polycation is immersed in colloidal suspensions of mww and bifer nanosheets under optimized conditions, achieving dense coverage of the substrate surface with the nanosheets. Subsequent repetition of this process in a desired sequence enables the design of various hierarchical films such as multilayers and superlattice films, which cannot be realized through any direct synthetic approach. Furthermore, this methodology can be extended to different types of zeolites or various other nanosheets, which expands the potential for zeolite-based materials with designed functionality for various applications. Such tailored structures with ultrathin thickness are regarded as more favorable for advanced applications, e g., high-precision and high-sensitivity sensors, ultrathin catalysts layers, adsorbents, and ion exchangers. This potential is expected to grow when other zeolite frameworks become available as exfoliated nanosheets,[73,74] especially like MFI with pores perpendicular to its layers enabling 3D transport.[60]

4. Experimental Section

Reagents: Tetrabutylammonium hydroxide solution (TBAOH, 10 wt.%, Wako special grade, FUJIFILM Wako Pure Chemical), poly(diallyldimethylammonium) chloride (PDDA, 20 wt.% in water, Sigma Aldrich), Rhodamine B (for fluorescence, Sigma Aldrich). These materials were used as purchased. Milli-Q filtered water was used throughout the experiments.

Preparation of the Suspensions of mww and bifer Zeolite Nanosheet: Layered zeolites MCM-56 and Al-ZSM-55 were prepared according to the previous reports.[53,54] The obtained MCM-56 (0.5 g) was dispersed in a TBAOH aqueous solution (10 wt.%, 30 cm^3). Then, deionized water (4.5 cm^3) was added to the mixture. After shaking for 48 h at 180 rpm, the mixture was first centrifuged at 20 krpm for 30 min to separate the swollen zeolite from the mixture. Then, the sediment was redispersed in deionized water (13 cm^3). After shaking for another 48 h, the mixture was centrifuged to separate the well-exfoliated zeolite nanosheet from the unexfoliated residue wherein the centrifuge speed was adjusted to accomplish this target. After washing the obtained nanosheets with deionized water two times, the mww nanosheets were dispersed in water to produce a suspension. The bifer nanosheet suspension was prepared from Al-ZSM-55 by a similar procedure.

Layer-by-layer Assembly of mww, bifer, and Their Hetero-Film: The typical layer-by-layer assembly procedure for depositing one zeolite layer consisted of four steps. Step I, a cleaned substrate was immersed in a solution of PDDA (20 g dm^{-3}, pH 9) for 15 min; step II, the substrate was taken out from the PDDA solution and carefully washed with deionized water, followed by flushing with N_2 gas stream; step III, the dried substrate was immersed in a suspension of the nanosheets at the desired concentration for appropriate time. Step IV was the same rinsing procedure as step II. Films with designed structures were fabricated layer-by-layer by repeating the procedures with desired nanosheets.

Materials Characterization: XRD patterns were recorded with a powder X-ray diffractometer (Rigaku, Ultima IV) using Cu Kα radiation (λ = 1.5405 Å). A zeta-potential and particle size analyzer (Otsuka Electronics, ELSZ-2) was employed to measure the zeta potential of the aqueous suspension. AFM (Hitachi High-Tech Science, AFM5000II) was used to characterize the topography of the nanosheets. In-plane XRD measurements were performed with synchrotron X-ray radiation (λ = 1.1991 Å) at line BL-6C of the Photon Factory, High Energy Accelerator Research Organization. FT-IR and UV–vis absorption spectra are recorded by Fourier transform infrared spectrometer (Perkin Elmer Instruments, Spectrum One) and UV–vis spectrometer (Shimadzu, SolidSpec-3700 DUV), respectively.

Adsorption Tests of Rhodamine B: Zeolite films such as multilayers and superlattice films based on mww and bifer nanosheets were fabricated on

a quartz glass substrate by layer-by-layer assembly process. Then, the fabricated samples were heated at 400 °C for 1 h and soaked in the Rhodamine B solution (0.1 mol dm^{-3}) for 24 h. After removal from the solution, the sample was carefully washed with copious amounts of deionized water to remove the dye from the surface, and UV–vis absorption spectra were recorded to estimate the amount of adsorbed dye.

Simulation of XRD Profile: XRD patterns of zeolite nanosheet films, in which the intersheet distance, *d*, is assumed to show Gaussian distribution, were simulated according to the following equations,

$$I(\theta) = \mathrm{Lp}(\theta)\,|F(\theta)|^2 \left[N + 2\sum_{n=1}^{N-1} (N-n)\, e^{-\frac{8\pi^2 n\alpha^2 \sin^2\theta}{\lambda^2}} \cos\left(4\pi n d \frac{\sin\theta}{\lambda}\right) \right] \quad (1)$$

$$F(\theta) = \sum n_j f_j \exp 2\pi i \left(\frac{2z_j \sin(\theta)}{\lambda} \right) \quad (2)$$

where *Lp* and *F(θ)* were Lorenz polarization factor and structure factor. The number of the stacked nanosheets, *N*, is 10 in this case and θ represents the scattering angle. The parameters of n_j, f_j, and z_j were multiplicity, atomic scattering factors, and the positions for Si(Al) and O atoms used on the mww and ferrierite structure representing bifer, respectively. The parameter, α, was the standard deviation of Gaussian distribution as a measure of structural disorder. Detailed calculation procedures for the structure factors have been described in the previous report.[10]

Supporting Information

Supporting Information is available from the Wiley Online Library or from the author.

Acknowledgements

The authors greatly acknowledge the support of the World Premier International Research Center Initiative (WPI), Ministry of Education, Culture, Sports, Science and Technology (MEXT), Japan, and CREST of the Japan Science and Technology Agency (JST) (Grant No. JPMJCR17N1 & JPMJCR22B1). C.W. acknowledges the Japan Society for the Promotion of Science (JSPS) fellowship (Grant No. P21036). The in-plane XRD measurements were performed with the approval of the Photon Factory Program Advisory Committee (Proposal No. 2022G501). The XRD simulations were conducted with the supercomputer at the Numerical Materials Simulator Station in NIMS. TEM images were recorded with the assistance of Dr. Daiming Tang in NIMS. Financing was provided with funds from the National Science Centre Poland, Grant no 2020/37/B/ST5/01258 (for W.J.R. and B.G.) and 2019/32/T/ST5/00188 (for J.G.).

Conflict of Interest

The authors declare no conflict of interest.

Data Availability Statement

The data that support the findings of this study are available from the corresponding author upon reasonable request.

Keywords

2D materials, dye adsorption, hierarchical structures, layer-by-layer assembly, open channels, unilamellar zeolite nanosheets

Received: September 20, 2023
Revised: December 19, 2023
Published online: January 28, 2024

[1] A. K. Geim, I. V. Grigorieva, *Nature* **2013**, *499*, 419.
[2] S. Z. Butler, S. M. Hollen, L. Cao, Y. Cui, J. A. Gupta, H. R. Gutiérrez, T. F. Heinz, S. S. Hong, J. Huang, A. F. Ismach, E. Johnston-Halperin, M. Kuno, V. V. Plashnitsa, R. D. Robinson, R. S. Ruoff, S. Salahuddin, J. Shan, L. Shi, M. G. Spencer, M. Terrones, W. Windl, J. E. Goldberger, *ACS Nano* **2013**, *7*, 2898.
[3] R. Ma, T. Sasaki, *Acc. Chem. Res.* **2015**, *48*, 136.
[4] R. Uppuluri, A. S. Gupta, A. S. Rosas, T. E. Mallouk, *Chem. Soc. Rev.* **2018**, *47*, 2401.
[5] P. Xiong, Y. Wu, Y. Liu, R. Ma, T. Sasaki, X. Wang, J. Zhu, *Energy Environ. Sci.* **2020**, *13*, 4834.
[6] P. Xiong, B. Sun, N. Sakai, R. Ma, T. Sasaki, S. Wang, J. Zhang, G. Wang, *Adv. Mater.* **2020**, *32*, 1902654.
[7] C. R. Dean, A. F. Young, I. Meric, C. Lee, L. Wang, S. Sorgenfrei, K. Watanabe, T. Taniguchi, P. Kim, K. L. Shepard, J. Hone, *Nat. Nanotechnol.* **2010**, *5*, 722.
[8] E. R. Kleinfeld, G. S. Ferguson, *Science* **1994**, *265*, 370.
[9] N. I. Kovtyukhova, P. J. Ollivier, B. R. Martin, T. E. Mallouk, S. A. Chizhik, E. V. Buzaneva, A. D. Gorchinskiy, *Chem. Mater.* **1999**, *11*, 771.
[10] T. Sasaki, Y. Ebina, T. Tanaka, M. Harada, M. Watanabe, G. Decher, *Chem. Mater.* **2001**, *13*, 4661.
[11] K. Matsuba, C. Wang, K. Saruwatari, Y. Uesusuki, K. Akatsuka, M. Osada, Y. Ebina, R. Ma, T. Sasaki, *Sci. Adv.* **2017**, *3*, e1700414.
[12] H. Yano, N. Sakai, Y. Ebina, R. Ma, M. Osada, K. Fujimoto, T. Sasaki, *ACS Appl. Mater. Interfaces* **2021**, *13*, 43258.
[13] N. Sakai, T. Sasaki, *Langmuir* **2022**, *38*, 12399.
[14] Y. Shi, M. Osada, Y. Ebina, T. Sasaki, *ACS Nano* **2020**, *14*, 15216.
[15] T. Yamaki, K. Asai, *Langmuir* **2001**, *17*, 2564.
[16] Y. Umemura, A. Yamagishi, R. Schoonheydt, A. Persoons, F. De Schryver, *J. Am. Chem. Soc.* **2002**, *124*, 992.
[17] K. Akatsuka, M. Haga, Y. Ebina, M. Osada, K. Fukuda, T. Sasaki, *ACS Nano* **2009**, *3*, 1097.
[18] L. Z. Wang, T. Sasaki, Y. Ebina, K. Kurashima, M. Watanabe, *Chem. Mater.* **2002**, *14*, 4827.
[19] J. Huang, R. Ma, Y. Ebina, K. Fukuda, K. Takada, T. Sasaki, *Chem. Mater.* **2010**, *22*, 2582.
[20] M. Osada, K. Akatsuka, Y. Ebina, H. Funakubo, K. Ono, K. Takada, T. Sasaki, *ACS Nano* **2010**, *4*, 5225.
[21] B.-W. Li, M. Osada, Y.-H. Kim, Y. Ebina, K. Akatsuka, T. Sasaki, *J. Am. Chem. Soc.* **2017**, *139*, 10868.
[22] N. Sakai, K. Kamanaka, T. Sasaki, *J. Phys. Chem. C* **2016**, *120*, 23944.
[23] W. Tu, Y. Zhou, Q. Liu, Z. Tian, J. Gao, X. Chen, H. Zhang, J. Liu, Z. Zou, *Adv. Funct. Mater.* **2012**, *22*, 1215.
[24] S. Ida, A. Takashiba, S. Koga, H. Hagiwara, T. Ishihara, *J. Am. Chem. Soc.* **2014**, *136*, 1872.
[25] J. L. Gunjakar, T. W. Kim, H. N. Kim, I. Y. Kim, S.-J. Hwang, *J. Am. Chem. Soc.* **2011**, *133*, 14998.
[26] W. Ma, R. Ma, C. Wang, J. Liang, X. Liu, K. Zhou, T. Sasaki, *ACS Nano* **2015**, *9*, 1977.
[27] P. Xiong, X. Zhang, H. Wan, S. Wang, Y. Zhao, J. Zhang, D. Zhou, W. Gao, R. Ma, T. Sasaki, G. Wang, *Nano Lett.* **2019**, *19*, 4518.
[28] Y. He, L. Jia, X. Lu, C. Wang, X. Liu, G. Chen, D. Wu, Z. Wen, N. Zhang, Y. Yamauchi, T. Sasaki, R. Ma, *ACS Nano* **2022**, *16*, 4028.
[29] N. Sakai, K. Fukuda, Y. Omomo, Y. Ebina, K. Takada, T. Sasaki, *J. Phys. Chem. C* **2008**, *112*, 5197.
[30] S. Werner, V. Wing-hei Lau, S. Hug, V. Duppel, H. Clausen-Schaumann, B. V. Lotsch, *Langmuir* **2013**, *29*, 9199.
[31] R. Ma, X. Liu, J. Liang, Y. Bando, T. Sasaki, *Adv. Mater.* **2014**, *26*, 4173.
[32] X. Cai, N. Sakai, T. C. Ozawa, A. Funatsu, R. Ma, Y. Ebina, T. Sasaki, *ACS Appl. Mater. Interfaces* **2015**, *7*, 11436.
[33] M. He, L. Kang, C. Liu, Z. Lei, Z.-H. Liu, *Mater. Res. Bull.* **2015**, *68*, 194.

[34] S. Ida, Y. Sonoda, K. Ikeue, Y. Matsumoto, *Chem. Commun.* **2010**, *46*, 877.
[35] M. Bai, X. Liu, T. Sasaki, R. Ma, *Nanoscale* **2021**, *13*, 4551.
[36] R. Ma, T. Sasaki, *Adv. Mater.* **2010**, *22*, 5082.
[37] V. Nicolosi, M. Chhowalla, M. G. Kanatzidis, M. S. Strano, J. N. Coleman, *Science* **2013**, *340*, 1226419.
[38] M. E. Davis, *Ind. Eng. Chem. Res.* **1991**, *30*, 1675.
[39] C. Martínez, A. Corma, *Coord. Chem. Rev.* **2011**, *255*, 1558.
[40] C. S. Cundy, P. A. Cox, *Chem. Rev.* **2003**, *103*, 663.
[41] P. van der Voort, K. Leus, E. de Canck, *Introduction to Porous Materials*, Wiley, Hoboken, NJ **2019**.
[42] F. Rouquerol, J. Rouquerol, K. S. W. Sing, P. Llewellyn, G. Maurin, *Adsorption by Powders and Porous Solids: Principles, Methodology and Applications*, Academic Press, Amsterdam **2013**.
[43] I. Fechete, Y. Wang, J. C. Védrine, *Catal. Today* **2012**, *189*, 2.
[44] A. F. Masters, T. Maschmeyer, *Microporous Mesoporous Mater.* **2011**, *142*, 423.
[45] J. Přech, P. Pizarro, D. P. Serrano, J. Čejka, *Chem. Soc. Rev.* **2018**, *47*, 8263.
[46] S. I. Zones, *Microporous Mesoporous Mater.* **2011**, *144*, 1.
[47] M. E. Leonowicz, J. A. Lawton, S. L. Lawton, M. K. Rubin, *Science* **1994**, *264*, 1910.
[48] L. Schreyeck, P. Caullet, J. C. Mougenel, J. L. Guth, B. Marler, *Microporous Mater.* **1996**, *6*, 259.
[49] B. Marler, H. Gies, *Eur. J. Mineral.* **2012**, *24*, 405.
[50] W. J. Roth, B. Gil, B. Marszalek, *Catal. Today* **2014**, *227*, 9.
[51] A. Corma, V. Fornes, S. B. Pergher, T. L. M. Maesen, J. G. Buglass, *Nature* **1998**, *396*, 353.
[52] W. J. Roth, B. Gil, W. Makowski, B. Marszalek, P. Eliasova, *Chem. Soc. Rev.* **2016**, *45*, 3400.
[53] W. J. Roth, T. Sasaki, K. Wolski, Y. Song, D.-M. Tang, Y. Ebina, R. Ma, J. Grzybek, K. Kałahurska, B. Gil, M. Mazur, S. Zapotoczny, J. Cejka, *Sci. Adv.* **2020**, *6*, eaay8163.
[54] W. J. Roth, T. Sasaki, K. Wolski, Y. Ebina, D.-M. Tang, Y. Michiue, N. Sakai, R. Ma, O. Cretu, J. Kikkawa, K. Kimoto, K. Kalahurska, B. Gil, M. Mazur, S. Zapotoczny, J. Čejka, J. Grzybek, A. Kowalczyk, *J. Am. Chem. Soc.* **2021**, *143*, 11052.
[55] S. L. Lawton, A. S. Fung, G. J. Kennedy, L. B. Alemany, C. D. Chang, G. H. Hatzikos, D. N. Lissy, M. K. Rubin, H. K. C. Timken, S. Steuernagel, D. E. Woessner, *J. Phys. Chem.* **1996**, *100*, 3788.
[56] T. F. Degnan Jr., C. M. Smith, C. R. Venkat, *Appl. Catal. A* **2001**, *221*, 283.
[57] W. J. Roth, B. Gil, W. Makowski, A. Sławek, J. Grzybek, M. Kubu, J. Čejka, *Chem. Mater.* **2016**, *28*, 3616.
[58] J. L. Wang, Y. Q. Fan, J. A. Jiang, Z. Wan, S. Y. Pang, Y. J. Guan, H. Xu, X. He, Y. H. Ma, A. S. Huang, P. Wu, *Angew. Chem., Int. Ed.* **2023**, *62*, e202304734.
[59] K. Ogorzaly, B. Gil, M. Mazur, W. Makowski, W. J. Roth, *Microporous Mesoporous Mater.* **2021**, *324*, 111300.
[60] W. J. Roth, T. Sasaki, K. Wolski, B. Gil, S. Zapotoczny, J. Čejka, M. Kubů, M. Mazur, Y. Ebina, N. Sakai, D.-M. Tang, R. Ma, *Inorg. Chem. Front.* **2023**, *10*, 1511.
[61] W. J. Roth, D. L. Dorset, G. J. Kennedy, *Microporous Mesoporous Mater.* **2011**, *142*, 168.
[62] B. Gil, W. J. Roth, W. Makowski, B. Marszalek, D. Majda, Z. Olejniczak, P. Michorczyk, *Catal. Today* **2015**, *243*, 39.
[63] M. Król, W. Mozgawa, W. Jastrzębski, *J. Porous Mater.* **2016**, *23*, 1.
[64] W. Mozgawa, M. Sitarz, M. Król, in *Molecular Spectroscopy – Experiment and Theory*, (Eds.: A. Koleżyński, M. Król), Springer International Publishing, Cham, Switzerland **2019**, pp. 457–481.
[65] T. Sasaki, Y. Ebina, K. Fukuda, T. Tanaka, M. Harada, M. Watanabe, *Chem. Mater.* **2002**, *14*, 3524.
[66] R. Arletti, G. Vezzalini, S. Quartieri, F. Di Renzo, V. Dmitriev, *Microporous Mesoporous Mater.* **2014**, *191*, 27.
[67] A. K. Patra, A. Dutta, M. Pramanik, M. Nandi, H. Uyama, A. Bhaumik, *Chem. Cat. Chem.* **2014**, *6*, 220.
[68] G. Gumilar, Y. V. Kaneti, J. Henzie, S. Chatterjee, J. Na, B. Yuliarto, N. Nugraha, A. Patah, A. Bhaumik, Y. Yamauchi, *Chem. Sci.* **2020**, *11*, 3644.
[69] L. Hu, V. T. Bui, S. Pal, W. Guo, A. Subramanian, K. Kisslinger, S. Fan, C.-Y. Nam, Y. Ding, H. Lin, *Small* **2022**, *18*, 2201982.
[70] E. J. Sonneveld, J. W. Visser, *J. Appl. Crystallogr.* **1975**, *8*, 1.
[71] S. B. Wang, H. Li, L. Y. Xu, *J. Colloid Interface Sci.* **2006**, *295*, 71.
[72] M. Rakanović, A. Vukojević, M. M. Savanović, S. Armaković, S. Pelemiš, F. Živić, S. Sladojević, S. J. Armaković, *Molecules* **2022**, *27*, 6582.
[73] V. Dudko, O. Khoruzhenko, S. Weiss, M. Daab, P. Loch, W. Schwieger, J. Breu, *Adv. Mater. Technol.* **2023**, *8*, 2200553.
[74] P. Loch, D. Schuchardt, G. Algara-Siller, P. Markus, K. Ottermann, S. Rosenfeldt, T. Lunkenbein, W. Schwieger, G. Papastavrou, J. Breu, *Sci. Adv.* **2022**, *8*, eabn9084.